Sensors & Diagnostics

ROYAL SOCIETY OF CHEMISTRY

PAPER

View Article Online
View Journal | View Issue

Cite this: *Sens. Diagn.*, 2025, **4**, 44

Enrichment of prostate-specific antigen using magnetic-silica antibody nanobioconjugates and fluorescence detection†

Tumelo Msutu[a] and Philani Mashazi *[ab]

Herein, we report the development of an immunosensor for the detection of prostate-specific antigen (PSA). The immunosensor platform was based on the immunometric sandwich protocol, using magnetic-silica nanoparticles for capture and pre-concentration of PSA. The preparation and application of the magnetic-silica nanobioconjugates and the use of phenylboronic acid for the immobilization of the capture antibody are the innovative steps of this report. The fluorescent sensing nanobioprobes contained 6% fluorescein in the fluorescein-doped silica nanoparticles. Silica nanoparticles can easily undergo alkaline dissolution for an enhanced fluorescence signal and thus ultrasensitive detection of PSA. The specificity of the immunosensor was achieved by the use of the anti-PSA monoclonal capture antibody (Ab_1) bioconjugated in an oriented manner onto phenylboronic acid functionalized magnetic-silica nanoparticles. Non-specific binding sites were blocked with glucose to yield Fe_3O_4@SiO_2-PBA-Ab_1/glucose. Ab_1 capture magnetic nanoparticles allowed for ease of separation using a magnet. For sensing, the polyclonal anti-PSA antibody (Ab_2) was bioconjugated onto fluorescein-doped silica nanoparticles to form FITC@SiO_2-PBA-Ab_2/glucose. PSA was selectively isolated, enriched and purified from the serum samples using a magnetic nanobioconjugate (Fe_3O_4@SiO_2-PBA-Ab_1/glucose). A sandwich immunoreaction was achieved with FITC@SiO_2-PBA-Ab_2/glucose binding to the captured PSA. The alkali hydrolysis resulted in the disintegration of the nanoparticle thus releasing FITC molecules for fluorescence detection. This resulted in signal amplification. The analytical performance of the proposed immunosensor showed an excellent linear relationship between the fluorescence signal intensity and the concentration of PSA ranging from 2.0 pg mL^{-1} to 100 ng mL^{-1}. The very low limit of detection (LOD) was 0.81 pg mL^{-1} and the limit of quantification (LOQ) was 2.46 pg mL^{-1}. The immunosensor also exhibited good specificity and selectivity to PSA with 98.0–102.7% recovery rates. The detection was accomplished in newborn calf serum samples representing real samples.

Received 23rd August 2024,
Accepted 3rd November 2024

DOI: 10.1039/d4sd00292j

rsc.li/sensors

1. Introduction

Prostate-specific antigen (PSA) is an androgen protease produced by both normal and cancerous cells.[1,2] It is used clinically as an effective biomarker for prostate cancer screening and monitoring.[3–5] Serum PSA levels below 4.0 ng mL^{-1} are considered normal for patients. However, PSA concentrations in the serum between 4.0 ng mL^{-1} and 10 ng mL^{-1} are considered to be a high risk for developing prostate cancer.[6,7] For these patients an invasive confirmatory test involving a tissue biopsy is used for confirmation. Patients with PSA levels greater than 10 ng mL^{-1} are at advanced developmental stages of prostate cancer. Therefore, precise quantification of PSA is important for the early diagnosis and monitoring the development of prostate cancer. Other methods for prostate cancer diagnosis are highly invasive and these include tissue biopsy, which may miss cancerous tissue, and digital rectal examination, which require skilled personnel for diagnosis. Biosensors are sensing systems capable of detecting ultra-low concentrations of PSA in bodily fluids. They improve the early detection of prostate cancer. Zhao *et al.*[8] designed a fluorescent immunosensor based on quantum dots as the detection probe. Quantum dots (QDs) contain heavy toxic metals like cadmium (Cd) in their preparation thus limiting their use due to the environmental effect[9] of heavy metals as pollutants. Herein, we report the use of fluorescein-5-isothiocyanate (FITC) as an organic fluorophore doped into a silica nanoparticle matrix for stability and used as a sensing nanobioprobe. The magnetic-silica nanoparticles with antibody bioconjugates were also

---

[a] *Department of Chemistry, Rhodes University, P.O. Box 94, Makhanda, 6140, South Africa. E-mail: p.mashazi@ru.ac.za*

[b] *Institute for Nanotechnology Innovation, Rhodes University, P.O. Box 94, Makhanda, 6140, South Africa*

† Electronic supplementary information (ESI) available: The materials, characterization and methods are further discussed in the ESI. See DOI: **https://doi.org/10.1039/d4sd00292j**

prepared and used as capture nanobioprobes. The non-toxic nature of magnetic-silica nanoparticles has been investigated for various medical applications.[10–12] Their advantageous use in biodetection is due to their facile synthesis, small size, stability, good dispersity and high magnetic moment.[11–13] The magnetic-silica nanoparticles provide an easy way to separate samples from solutions using a magnet.[14–16] Magnetic-silica capture nanobioprobes contain iron oxide nanoparticles at the core and a silica shell. Iron oxide nanoparticles (Fe_3O_4NPs) alone are used in biomedical applications for magnetic resonance imaging (MRI), biomolecular separation, and for targeted drug delivery.[10–18] This is due to their superparamagnetic properties, controllable nanoparticle size, and high specific surface area.[10–19] Bare Fe_3O_4NPs are also prone to agglomeration, air oxidation, and biodegradation.[20–22] To overcome such limitations, surface functionalization has been shown to be successful[19–22] and silica (SiO_2) is a widely used coating shell.[11,12,15,20–25] SiO_2 provides unique properties such as good stability, hydrophilicity, biocompatibility, and ease of surface modification, and helps prevent unwanted interactions with the magnetic core.[19–26] Iron oxide–silica nanoparticles have been functionalized by direct covalent immobilization with phenylboronic acid for oriented antibody immobilization.[25] The boronic acid functional groups form strong covalent boronate ester bonds with the *N*-glycans on the Fc region of the antibody[27,28] exposing antigen binding sites.

The use of phenylboronic acid for antibody immobilization is not widely reported even though it offers oriented immobilization. This is because antibodies with *N*-glycans are not widely produced. In this work, we exploit *N*-glycosylated antibodies for oriented immobilization. Both anti-PSA monoclonal (Ab_1) and polyclonal (Ab_2) antibodies were respectively immobilized onto magnetic nanoparticles for capture and enrichment of PSA and onto FITC-doped silica nanoparticles for fluorescence sensitive detection. A sandwich-type fluorescence immunoassay was developed and assessed for selective detection of PSA. The novelty of this work is in the preparation of the magnetic-silica nanobioconjugates and the use of phenylboronic acid for the immobilization of the capture antibody. Furthermore, the detection of PSA using sandwich immunoassay with fluorescent dye-doped silica nanoparticles and magnetic-silica nanoparticles (magnetic separation) for analyte capture and enrichment was demonstrated. The use of the magnetic-silica–Ab_1 and FITC-doped silica–Ab_2 nanoparticles is to our knowledge reported here for the first time.

2. Experimental

2.1 Materials and reagents

Iron(III) chloride ($FeCl_3 \cdot 2H_2O$), sodium oleate, oleic acid (90%), 1-octadecene (90%), tetraethyl orthosilicate (TEOS, 99.9%), sodium chloride (NaCl), mouse anti-human IgG antibody (IgG), and 4-(1,1,3,3-tetramethylbutyl)-phenyl polyethylene glycol (Triton X-100) were purchased from Sigma-Aldrich (USA). Absolute ethanol (98.6%, w/v), sodium dihydrogen phosphate (NaH_2PO_4), disodium hydrogen phosphate (Na_2HPO_4), and anhydrous D-glucose were purchased from SAARChem (South Africa). Cyclohexane (99.5%) and toluene were purchased from Merck (Germany). Hexan-1-ol was purchased from B&M Scientific (South Africa). Ammonium hydroxide (NH_4OH, 25% wt) was purchased from Minema Chemicals (South Africa). The triethoxysilanepropyl-3-amido phenylboronic acid (TES-PBA) precursor was prepared and characterized as previously reported.[29] Prostate-specific antigen (PSA), mouse anti-human prostate-specific antibody (Ab_1, 7820-0370) and sheep anti-human prostate-specific antibody (Ab_2, 7820-0154) were purchased from Bio-Rad Laboratories (USA).

A coupling buffer, phosphate buffered saline (PBS, pH 7.4, 10 mM), was prepared using 0.63 g disodium hydrogen phosphate (Na_2HPO_4) and 60 mg sodium dihydrogen phosphate (NaH_2PO_4) in 400 mL of distilled water. A washing buffer (PBST, pH 7.4, 10 mM) was prepared using 1.2 g disodium hydrogen phosphate (Na_2HPO_4), 0.12 g sodium dihydrogen orthophosphate (NaH_2PO_4), and 100 μL of Tween 20 in 100 mL of ultra-pure Millipore water. All reagents and solvents in this study were of analytical grade and used as received from the supplier. Ultra-pure water with a resistivity of 18 MΩ cm (at 25 °C) was obtained from a Milli-Q water purification system (Millipore Corp. Bedford, MA, USA) and was used throughout the experiments. The synthesis of 6% FITC@SiO_2NPs and bioconjugation of Ab_2 as sensing nanobioprobes were performed following our previous work using FITC@SiO_2-PBA-Ab_2/glucose.[29] The functionalization with the boronic group and antibody bioconjugation are reported in the ESI.†

2.2 Apparatus and instrumentation

Infra-red spectra were collected on a Perkin-Elmer Universal ART sampling accessory spectrum 100 FT-IR spectrometer. Zeta-potential measurements were carried out on a Malvern Zetasizer Nano series, Nano ZS90 series S equipped with a 633 nm He/Ne laser. Scanning electron microscopy (SEM) and energy dispersive X-ray spectroscopy (SEM-EDS) and elemental mapping were carried out using an INCA penta FET coupled to the VAGA TESCAM using 20 kV accelerating voltage. The X-ray powder diffraction (XRD) patterns were recorded on a Bruker D8 Discover equipped with a Lynx Eye detector, using Cu-Kα radiation (1.5405 Å, nickel filter). The data were collected in the range from 2θ = 10° to 90°, scanning at 1° min^{-1} with a filter time-constant of 2.5 seconds per step and a slit width of 6.0 mm. Samples were placed on a silicon wafer slide. The XRD data were treated using the freely available Eva (evaluation curve fitting) software. Baseline correction was performed on each diffraction pattern by subtracting a spline fitted to the curve background. UV-visible (UV-vis) spectroscopy analysis was performed on a SHIMADZU UV-2550 spectrometer. The fluorescence spectra were recorded using a SpectraMax multi-mode spectrofluorometer and Synergy MX microplate reader.

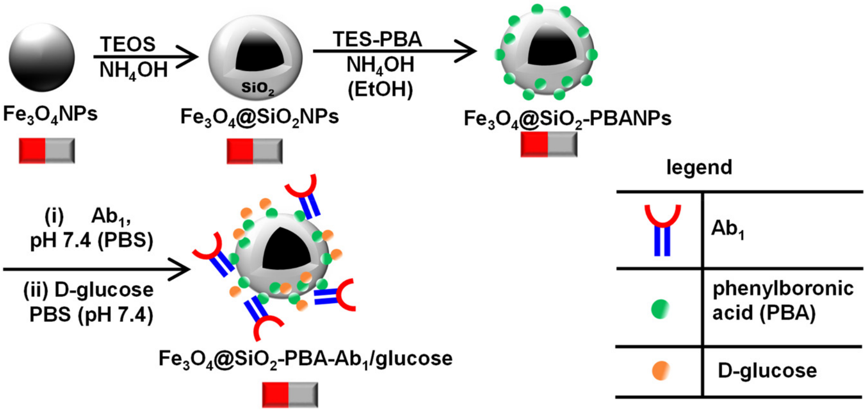

Scheme 1 Step-by-step preparation of the $Fe_3O_4@SiO_2$-PBA-Ab_1/glucose capture nanobioconjugates.

2.3 Preparation of magnetic-silica–Ab_1 nanoparticles, Scheme 1

2.3.1 Synthesis of oleic-capped magnetic nanoparticles (Fe_3O_4NPs). Fe_3O_4NPs were prepared following a reported method with some modifications.[23] In a typical synthesis procedure, iron(III) chloride (1.25 g, 4.62 mmol) was dissolved in distilled water (10 mL). Sodium oleate (5.22 g, 17.2 mmol) was added into the mixture under stirring at room temperature. Ethanol (12.5 mL) and *n*-hexane (20.0 mL) were added into the mixture and allowed to react at 85 °C for 4 hours. The colour of the mixture changed from deep maroon to dark brown. The resulting solution was separated using a separating funnel. The sticky reddish-brown organic layer obtained was an $Fe(oleate)_3$ precursor. It was washed with deionized water and oven-dried overnight at 80 °C. The sticky $Fe(oleate)_3$ precursor (3.0 g, 3.4 mmol) was dispersed in oleic acid (2.0 mL) and 1-octadecene (7.5 mL). The mixture was degassed under nitrogen gas for 30 minutes at room temperature. The temperature was increased by 10 °C every 5 minutes up to 320 °C. The reaction was maintained at 320 °C under a flowing stream of nitrogen gas for 45 minutes. The resulting solution was cooled at room temperature. Ethanol (10 mL) was added to precipitate the oleic-capped Fe_3O_4NPs that were collected using a magnet. Fe_3O_4NPs were suspended in hexane and ethanol several times. They were then magnetically separated to obtain clean Fe_3O_4NPs.

FT-IR (ATR, τ_{max}/cm^{-1}): 2918 (C–H), 2849 (C–H), 1545 (C–C), 1409 (C–H), 562 (Fe–O).

2.3.2 Preparing silica coated Fe_3O_4NPs ($Fe_3O_4@SiO_2$NPs). A water-in-oil (W/O) reverse microemulsion method was used to encapsulate Fe_3O_4NPs in the silica shell to form $Fe_3O_4@SiO_2$ nanoparticles. The microemulsion solution was obtained by mixing *n*-hexanol (1.8 mL), Fe_3O_4NPs (2.0 mg mL^{-1}), cyclohexane (15 mL), Triton X-100 (4.5 mL), and water (1.5 mL) in a reaction flask. The mixture was stirred for 45 minutes to form a microemulsion. A transparent golden-yellow solution formed. NH_4OH (200 μL, 25%) and TEOS (25.0 μL, 0.12 mmol) were mixed together and the reaction was allowed to continue for 6 hours. Additionally, TEOS (10.0 μL, 0.056 mmol) was added every 2 hours and six additions were used to grow a silica shell. After the last addition of TEOS, the mixture was stirred for 12 hours at room temperature, forming $Fe_3O_4@SiO_2$NPs. Acetone (20 mL) was added to break the microemulsion. Isolating the $Fe_3O_4@SiO_2$NPs was done by pH adjustment to pH 2 with cooling in liquid nitrogen. $Fe_3O_4@SiO_2$NPs were washed with water and ethanol (1 : 3 volume) solution and collected by magnetic separation. The magnetic-silica nanoparticles were dried in the oven overnight at 50 °C and collected as a brown powder.

FT-IR (ATR, τ_{max}/cm^{-1}): 3285 (O–H), 1046 (Si–O–Si), 940 (Si–O), 797 (Si–OH), 562 (Fe–O).

2.3.3 Boronic acid functionalization of magnetic-silica nanoparticles ($Fe_3O_4@SiO_2$-PBANPs). TES-PBA (20 mg, 80 μmol) dissolved in 5.0 mL ammonium solution was allowed to react. After 10 minutes, $Fe_3O_4@SiO_2$NPs (20 mg) dissolved in a mixture of (9 : 1) dry EtOH and toluene were added. The mixture reacted for 24 h at room temperature and resulted in the phenylboronic functionalized magnetic-silica nanoparticles ($Fe_3O_4@SiO_2$-PBANPs). A magnet was used to separate the product after several washing steps with a 1 : 1 mixture of water and ethanol. The product was dried at 50 °C for 48 h.

FT-IR [(ATR), τ_{max}/cm^{-1}]: 3872 (N–H), 1649 (C=O), 1541 (N–H), 1386 (B–O), 1056 (Si–O–Si), 949 (Si–O), 785 (Si–OH), 567 (Fe–O).

2.3.4 Bioconjugation of the Ab_1 capture antibody onto $Fe_3O_4@SiO_2$-PBANPs. $Fe_3O_4@SiO_2$-PBANPs (2.0 mg mL^{-1}) suspended in cold PBS buffer (2.0 mL, pH 7.4, 10 mM) were reacted with the monoclonal anti-PSA antibody (50 μL, 1.0 mg mL^{-1}) for 6 hours at 4 °C under slow continuous stirring. The antibody-modified magnetic-silica nanoparticles ($Fe_3O_4@SiO_2$-PBA-Ab_1) were washed with cold PBS (pH 7.4) to remove the unbound antibodies. The unreacted boronic acid sites were blocked by reacting the purified $Fe_3O_4@SiO_2$-PBA-Ab_1 with D-glucose (50 μg mL^{-1}) in cold PBS buffer (pH 7.4, 10 mM). After 2 hours, the mixture was separated using a magnet and washed with cold PBS buffer (pH 7.4, 10 mM) to yield $Fe_3O_4@SiO_2$-PBA-Ab_1/glucose. The resulting product was kept at 4 °C before use.

FT-IR [(ATR), τ_{max}/cm^{-1}]: 3355 (N–H), 1639 (C=O, amide I), 1546 (C=O, amide II), 1390 (B–O), 1064 (Si–O–Si), 985 (Si–O), 795 (Si–OH), 567 (Fe–O).

The Bradford assay was used for the quantification of the antibody (Ab_1) bioconjugated onto Fe_3O_4@SiO_2-PBANPs to yield Fe_3O_4@SiO_2-PBA-Ab_1. The experimental conditions are outlined in the ESI.†

2.4 Immunoassay procedure for detection of PSA

The capture nanobioconjugates, Fe_3O_4@SiO_2-PBA-Ab_1/glucose (100 μL, 100 μg mL^{-1}), were added into 50 μL of spiked serum in pH 7.4 PBS with different concentrations of PSA. The mixture was gently shaken for 50 min at room temperature. This resulted in the capture of PSA, Fe_3O_4@SiO_2-PBA-Ab_1<PSA, which was magnetically separated. The captured PSA, Fe_3O_4@SiO_2-PBA-Ab_1<PSA was washed with PBS (pH 7.4) three times. The sensing nanobioprobes, FITC@SiO_2-PBA-Ab_2/glucose (100 μL, 200 μg mL^{-1}), were added. The mixture was incubated in PBS (pH 7.4) with gentle shaking for 50 min at room temperature. Upon magnetic separation, the sandwich immunoassay (Fe_3O_4@SiO_2-PBA-Ab_1<PSA>Ab_2-PBA-SiO_2@FITC) was obtained. The isolated immunoassay was washed three times with cold PBS buffer (pH 7.4) and a magnet was used for separation. The sandwiched PSA will result in the capture of the fluorescent nanoparticles and they were magnetically separated. The isolated Fe_3O_4@SiO_2-PBA-Ab_1<PSA>Ab_2-PBA-SiO_2@FITC immunocomplex was dispersed in 50 μL of PBS buffer (pH 7.4,10 mM). NaOH (20 μL, 10 mM) was added and incubated at 30 °C. After 20 min, the fluorescence was measured at 480 nm excitation wavelength. The total assay time was 120 min and the fluorescence signal was recorded for each concentration of PSA.

3. Results and discussion

3.1 Synthesis and characterization of Fe_3O_4@SiO_2-PBA-Ab_1/glucose

Magnetic-silica nanobioconjugates were prepared and accomplished following several steps. Initially, the synthesis of the stable magnetite (Fe_3O_4NPs) nanoparticles was done by (a) the thermal decomposition of the Fe(oleate)$_3$ precursor to form a wüstite (Fe–O) nanomaterial and (b) the oxidation of Fe–O to form the Fe_3O_4 phase.[14,30,31] A quaternary water-in-oil (W/O) reverse microemulsion method afforded a coat of Fe_3O_4NPs with a silica shell to yield Fe_3O_4@SiO_2NPs. Oleic acid-capped magnetic nanoparticles were coated with the silica shell *via* ligand exchange of the oleic ligands and hydrolyzed tetraethyl orthosilicate (TEOS). TEOS undergoes polycondensation, forming Fe–O–Si and Si–O–Si bonds resulting in a silica shell.[19,32] The Fe_3O_4@SiO_2NPs were surface functionalized with triethoxysilanepropyl-3-amido phenylboronic acid (TES-PBA) to form Fe_3O_4@SiO_2-PBANPs. The Fe_3O_4@SiO_2-PBANPs were bioconjugated with Ab_1 and non-specific binding sites were blocked with D-glucose to yield Fe_3O_4@SiO_2-PBA-Ab_1/glucose nanobioconjugates. The step-by-step preparation and characterization of Fe_3O_4@SiO_2-PBA-Ab_1/glucose were carried out.

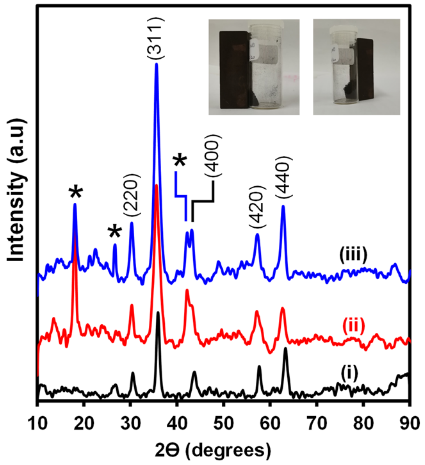

Fig. 1 XRD diffractograms of (i) Fe_3O_4NPs, (ii) Fe_3O_4@SiO_2NPs, and (iii) Fe_3O_4@SiO_2-PBANPs. The insert exhibits the photographs of Fe_3O_4@SiO_2NPs and Fe_3O_4@SiO_2-PBANPs in the presence of the magnetic field.

Fig. 1 shows the XRD diffractograms of (i) Fe_3O_4NPs, (ii) Fe_3O_4@SiO_2NPs, and (iii) Fe_3O_4@SiO_2-PBANPs. The diffractogram in Fig. 1(i) showed the formation of the Fe_3O_4NPs. The diffraction patterns are observed at 2θ values of 30.6°, 35.8°, 43.8°, 57.7°, and 63.2° which are indicative of a crystalline cubic spinel structure of the magnetite (Fe_3O_4).[19,33,34] The diffraction patterns show the characteristic of magnetite which were indexed to the following Miller Indices (220), (311), (400), (420), and (440).[25,35] The diffraction patterns matched well with the Fe_3O_4NPs for the JCPDS-International Centre (JCPDS file No. 19-0629). Similarly, the same peaks are observed for the functionalized magnetic-silica nanoparticles, Fe_3O_4@SiO_2NPs and Fe_3O_4@SiO_2-PBANPs, with a new peak observed at 2θ = 18.1° from the amorphous SiO_2 as shown in Fig. 1(ii) and (iii). This indicated that Fe_3O_4NPs were stable after the formation of the silica shell and post-surface functionalization with TES-PBA. The crystalline phase of the Fe_3O_4NPs after silica shell coating and surface functionalization remained intact. The average crystal size of the Fe_3O_4NP core, obtained by calculation using the Debye–Scherrer equation was calculated to be 8.7 nm for Fe_3O_4NPs, 15.9 nm for Fe_3O_4@SiO_2NPs, and 16.5 nm for Fe_3O_4@SiO_2-PBANPs. The increase in particles size was due to the silica shell coating the Fe_3O_4NP core. The functionalization with TES-PBA did not result in the increase in the particle size and this is due to the thin layer of TES-PBA forming Fe_3O_4@SiO_2-PBANPs. The nanoparticles retained their magnetic properties.

Fig. 2 shows the TEM micrographs and size distribution histograms of (a) Fe_3O_4NPs, (b) Fe_3O_4@SiO_2NPs, and (c) Fe_3O_4@SiO_2-PBANPs. The TEM micrographs of the nanoparticles were spherical and exhibited monodispersity. For Fe_3O_4NPs, the average diameter sizes were 10 ± 2 nm, clumping together as shown in Fig. 2(a). The clumping together or self-association of magnetic nanoparticles was due to the magnetic properties of the iron oxide. A 5 nm increase in the

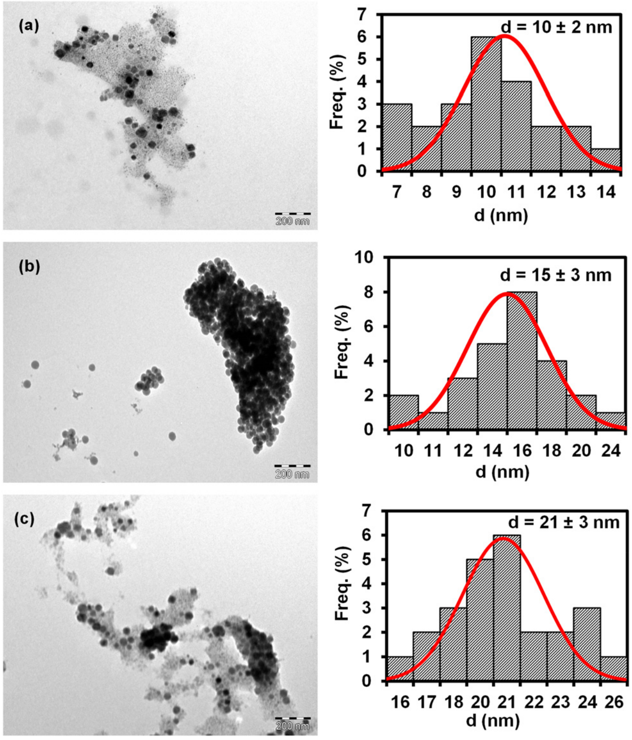

Fig. 2 TEM images and corresponding size distribution histograms of (a) Fe_3O_4NPs, (b) Fe_3O_4@SiO_2NPs, and (c) Fe_3O_4@SiO_2-PBANPs.

particle size diameter to 15 ± 3 nm for Fe_3O_4@SiO_2NPs is shown in Fig. 2(b). A 5 nm size increase was attributed to the silica shell formation. The magnetic properties remained even after coating with a silica shell. The reverse water-in-oil (W/O) microemulsion method induced the surfactant Triton-X100 to surround droplets that contained the Fe_3O_4NPs and subsequent coating of silica *via* hydrolysis of the TEOS precursor.[34] A 6 nm average particle size increase was observed after functionalization with phenylboronic acid to form Fe_3O_4@SiO_2-PBANPs. The average particle size distribution of Fe_3O_4@SiO_2-PBANPs was 21 ± 3 nm as shown in Fig. 2(c). The increase in the particle size diameter was due to the introduction of TES-PBA onto the silica surface. Furthermore, the particle size distribution of Fe_3O_4@SiO_2-PBA-Ab_1 as compared to the Fe_3O_4@SiO_2-PBANPs showed no size variations. The antibody being a protein molecule does not appear in the TEM measurement. The successive increase in particle size diameter at each stage of functionalization successfully confirms the coating with the silica shell, TES-PBA and Ab_1.

Further characterization of the as-prepared magnetic nanoparticles was performed by EDS-SEM, FT-IR analyses, and zeta-potential measurements. Fig. 3 shows the EDS spectra with corresponding SEM images of (a) Fe_3O_4NPs, (b) Fe_3O_4@SiO_2NPs, and (c) Fe_3O_4@SiO_2-PBANPs. Fe_3O_4NPs in Fig. 3(a) showed the presence of Fe K (33.9%), O K (27.8%), and C K (38.3%) confirming the formation of iron oxide nanoparticles. The carbon (C K) was from the oleic acid (C–H) chains from the iron(II) oleate precursor. After modifying with the silica shell, the EDX spectrum in Fig. 3(b) showed the emergence of the Si K. The elemental composition showed Fe K (29.5%), Si K (20.1%) and O K (50.4%). The increase in O K from 27.8% to 50.4% is due to the silica (SiO_2) shell, and the Fe K decrease from 33.9% to 29.5% further confirms the formation of the silica (SiO_2) shell. The presence of Si K and increased O peaks confirms the successful silica coating of magnetic nanoparticles. The C K disappeared after the formation of the silica shell. After surface functionalization with TES-PBA to yield Fe_3O_4@SiO_2-PBANPs, the appearance of the boron (B K) peak (6.6%) was observed in Fig. 3(c). Further, the presence of the N K peak (3.8%) is due to the amide bond from TES-PBA and the C K peak (5.0%) from TES-PBA. The corresponding scanning electron microscopy (SEM) images and the EDX spectra showed the smooth particles of Fe_3O_4NPs. These became rough and porous after silica shell formation and functionalization with phenylboronic acid.

Fig. 4 shows the FT-IR spectra of (i) Fe_3O_4NPs, (ii) Fe_3O_4@SiO_2NPs, (iii) Fe_3O_4@SiO_2-PBANPs, and (iv) Fe_3O_4@SiO_2-PBA-Ab_1. The FT-IR spectrum of Fe_3O_4NPs in Fig. 4(i) shows the aliphatic C–H asymmetric and symmetric stretching bands at 2918 cm^{-1} and 2849 cm^{-1}. The peaks at 1545 cm^{-1} and 1409 cm^{-1} are attributed to asymmetric and symmetric ($-COO^-$) stretching vibrations, due to the carboxylates with Fe ions of Fe_3O_4NPs. Oleic acid (OA) is a stabilizer of Fe_3O_4NPs and is chemically bound to the magnetite (Fe_3O_4NPs) *via* oxygen atoms of the carboxylic acid functional group. An intense (Fe–O) peak is also observed at 562 cm^{-1} confirming the successful synthesis and coating of Fe_3O_4NPs with oleic acid. Then, it was followed by the coating with SiO_2 shell to form Fe_3O_4@SiO_2NPs. This is to enable the stability of the nanoparticles. After the formation of the silica shell, the peaks at 1710 cm^{-1}, 1545 cm^{-1}, and 1409 cm^{-1} disappeared as shown in Fig. 4(ii). This was due to the ligand exchange between TEOS and oleic acid ligands to yield Fe_3O_4@SiO_2 core shell nanoparticles. Additionally, a broad (O–H) peak is observed at 3285 cm^{-1}. Other peaks at 1046 cm^{-1}, 940 cm^{-1}, and 797 cm^{-1} appeared due to the asymmetric stretching vibration bands of siloxane (Si–O–Si), (Si–O), and silanol (Si–OH) groups, respectively. A decrease in the (Fe–O) peak is observed at 562 cm^{-1}. This confirmed the successful synthesis of the Fe_3O_4@SiO_2NPs. Surface functionalization of the magnetic-silica nanoparticles was achieved using TES-PBA through a covalent attachment forming siloxane bond. Fig. 4(iii) shows the Fe_3O_4@SiO_2-PBANP spectrum which exhibits an N–H stretching peak at 3872 cm^{-1} corresponding to the N–H bending at 1541 cm^{-1} of the amide bond of TES-PBA. The (C=O) absorption peak at 1649 cm $^{-1}$ and the emergence of the absorption peak of the (B–O) vibrational stretching at 1386 cm^{-1} are observed. These indicate the successful surface modification of Fe_3O_4@SiO_2NPs with TES-PBA onto the silica layer. The Fe_3O_4@SiO_2-PBANPs were later reacted with anti-PSA-mAb (Ab_1) to form Fe_3O_4@SiO_2-PBA-Ab_1. The immobilization of the antibody was achieved through cyclic boronate ester bonds between the *cis*-diol of

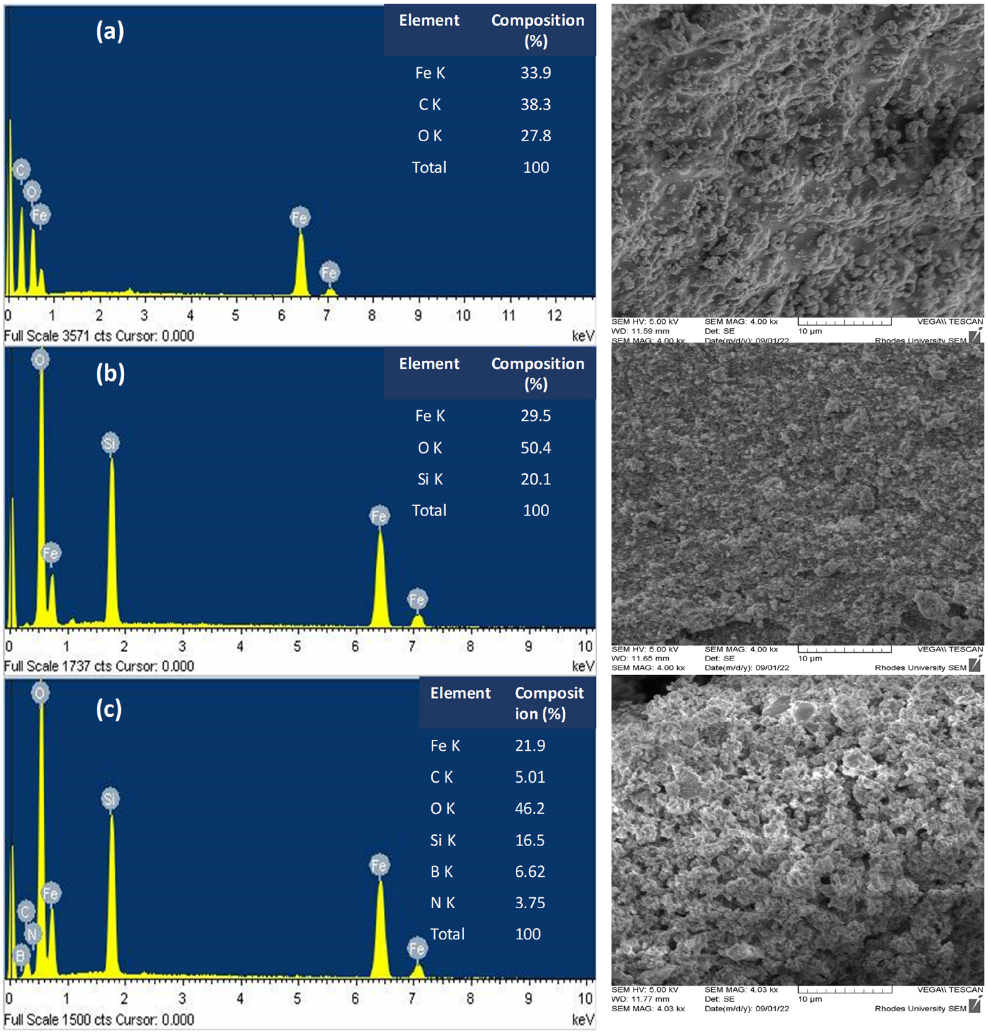

(a)

Element	Composition (%)
Fe K	33.9
C K	38.3
O K	27.8
Total	100

(b)

Element	Composition (%)
Fe K	29.5
O K	50.4
Si K	20.1
Total	100

(c)

Element	Composition (%)
Fe K	21.9
C K	5.01
O K	46.2
Si K	16.5
B K	6.62
N K	3.75
Total	100

Fig. 3 Energy dispersive X-ray (EDX) spectra with their corresponding SEM images for (a) Fe_3O_4NPs, (b) Fe_3O_4@SiO_2NPs, and (c) Fe_3O_4@SiO_2-PBANPs.

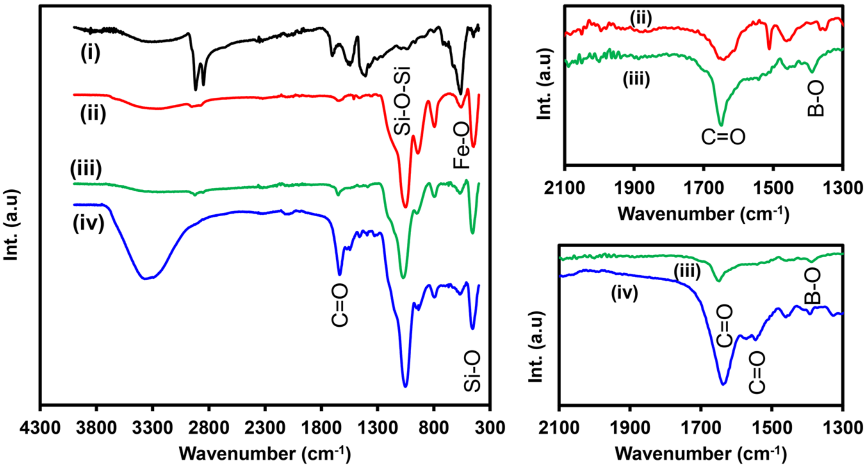

Fig. 4 FT-IR spectra of (i) Fe_3O_4NPs, (ii) Fe_3O_4@SiO_2NPs, (iii) Fe_3O_4@SiO_2-PBANPs, and (iv) Fe_3O_4@SiO_2-PBA-Ab_1 (enlarged 1300–2100 cm^{-1} for B–O, C=O).

the *N*-glycan moieties on the Fc region of the antibody and the (–OH) groups on the phenylboronic acid. The boronic acid bioconjugation method helps target the heavy chain antibody and this maintains the orientation of the antibody for enhanced antigen binding. Fig. 4(iv) shows the FT-IR spectrum of Fe_3O_4@SiO_2-PBA-Ab_1 and the appearance of intense stretching vibrational peaks of the (C=O, amide I) and (C=O, amide II) cyclic ester bonds of the anti-PSA antibody at 1639 cm^{-1} and 1546 cm^{-1} is observed. The absorption peak at 3355 cm^{-1} is assigned to the presence of the NH_2 from the antibody. The shift of the B–O peak from 1386 cm^{-1} to 1390 cm^{-1} of the boronic acid confirmed the successful bioconjugation of the antibody to the phenylboronic acid. This confirms the successful preparation of Fe_3O_4@SiO_2-PBA-Ab_1 capture nanobioconjugates.

Fig. 5 shows the zeta potential (ζ, mV) plot obtained at various pH values ranging from 2 to 10 in PBS, 10 mM for (i) Fe_3O_4NPs, (ii) Fe_3O_4@SiO_2NPs, (iii) Fe_3O_4@SiO_2-PBANPs, and (iv) Fe_3O_4@SiO_2-PBA-Ab_1. Fig. 5(i) shows zeta potential changes on Fe_3O_4NPs and a negative increasing trend of zeta potential values up to −30 mV as the pH values increase. The negative increase in the zeta potential value is due to the deprotonation of the surface hydroxyl (OH) and negative surface charge. The zeta potential was −23.8 mV at pH 7.0. After coating with the silica shell as shown in Fig. 5(ii) for Fe_3O_4@SiO_2NPs, the zeta potential value started at +2.0 mV at pH 2. As the pH increased, the zeta potential values became negative and increased negatively up to −43.2 mV at pH 10. The isoelectric point (IEP) was observed at pH 2.3. At pH 7.0, the zeta potential was −32.2 mV. The negative increase in the zeta potential was due to the deprotonation of the silanol (Si–OH) groups of the silica shell. After surface functionalization with TES-PBA as shown in Fig. 5(iii), a negative increase in the zeta potential charge from +24.0 mV at pH 3 to −40.0 mV at pH 10 was observed. The isoelectric point was observed at pH 5.4. The zeta potential charge was due to the deprotonation of the (B–OH) hydroxyl groups from TES-PBA. A zeta potential of −30.0 mV was obtained at pH 7.0. Fig. 5(iv) shows the pH effect on Fe_3O_4@SiO_2-PBA-Ab_1. A negative increase in the zeta potential from +25.0 mV at pH 2.0 to −23 mV at pH 10 was observed. An isoelectric point was obtained at pH 6.4 and the zeta potential value of −3.7 mV was observed at pH 7.0. The observed changes in zeta potential values at different pH solutions confirm the successful step-by-step modification and bioconjugation of the Ab_1 to form Fe_3O_4@SiO_2-PBA-Ab_1.

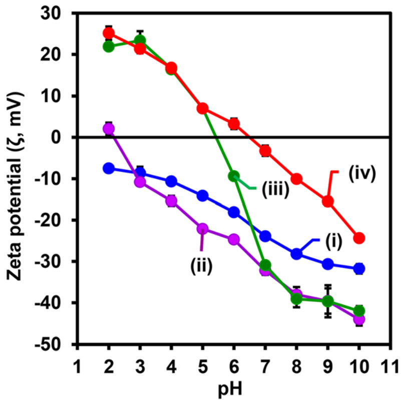

Fig. 5 Zeta potential (ζ, mV) *vs.* pH (2–10, PBS, 10 mM) for (i) Fe_3O_4NPs, (ii) Fe_3O_4@SiO_2NPs, (iii) Fe_3O_4@SiO_2-PBANPs, and (iv) Fe_3O_4@SiO_2-PBA-Ab_1.

The Bradford assay was used for protein quantification of Ab_1 bioconjugated onto Fe_3O_4@SiO_2–PBANPs. The calibration curve at different BSA concentrations was used to measure the protein solution before and after conjugation. The UV-vis absorbance measurements were performed at 595 nm for BSA and the same wavelength was used for determining the protein (Ab_1) concentration. The protein amount bioconjugated onto Fe_3O_4@SiO_2-PBANPs to form Fe_3O_4@SiO_2-PBA-Ab_1 was calculated by subtracting the determined concentration of the supernatant from the initial concentration in solution of Ab_1. After bioconjugation, the percentage of the conjugation efficiency (%CE) was calculated using eqn (1) below:

$$\%\mathrm{CE} = \frac{[\mathrm{Ab}_1]_0 - [\mathrm{Ab}_1]_\mathrm{f}}{[\mathrm{Ab}_1]_0} \times 100\% \tag{1}$$

where $[Ab_1]_0$ and $[Ab_1]_f$ show the initial and final concentrations of Ab_1 in the supernatant. The %CE was found to be 71.9% corresponding to the amount of protein conjugated onto Fe_3O_4@SiO_2-PBA to form Fe_3O_4@SiO_2-PBA-Ab_1. The Bradford assay details are shown in ESI† Fig. S1 and confirmed the successful preparation of Fe_3O_4@SiO_2-PBA-Ab_1 nanobioconjugates.

3.2 Evaluation and optimization of PSA capture and fluorescence detection

In the proposed immunosensor, Fe_3O_4@SiO_2-PBA-Ab_1/glucose nanobioconjugates were used to capture PSA from the sample solution as the first immunoreaction. Then, FITC@SiO_2-PBA-Ab_2/glucose fluorescence nanobioprobes were added to recognize the captured PSA by the second immunoreaction, forming the sandwich immunocomplex, Fe_3O_4@SiO_2-PBA-Ab_1<PSA>Ab_2-PBA@SiO_2@FITC. Scheme 2 shows the capture and fluorescence detection of PSA.

Fig. 6 shows the fluorescence emission spectra of the magnetic nanoparticles for (i) Fe_3O_4@SiO_2-PBA-Ab_1<PSA and (ii) Fe_3O_4@SiO_2-PBA-Ab_1<PSA>Ab_2-PBA-SiO_2@FITC. In Fig. 6(i), no fluorescence absorption was observed for Fe_3O_4@SiO_2-PBA-Ab_1<PSA (after the PSA was captured). The same spectrum was observed in the absence of PSA. Absorption and fluorescence emission intensities were observed when PSA and FITC@SiO_2-PBA-Ab_2 were introduced in the system as shown in Fig. 6(ii). This confirmed that the sandwich immunoassay occured. The use of a magnet allowed for the separation of a sandwich immunoassay (Fe_3O_4@SiO_2-PBA-Ab_1<PSA>Ab_2-PBA-SiO_2@FITC).

The concentration of the Fe_3O_4@SiO_2-PBA-Ab_1/glucose capture and FITC@SiO_2-PBA-Ab_1/glucose sensing nanobioprobes and the effect of the incubation time after PSA antigen capture were optimized. Both the concentration and incubation time parameters affect the sensitivity of the immunoassay. Fig. S2†

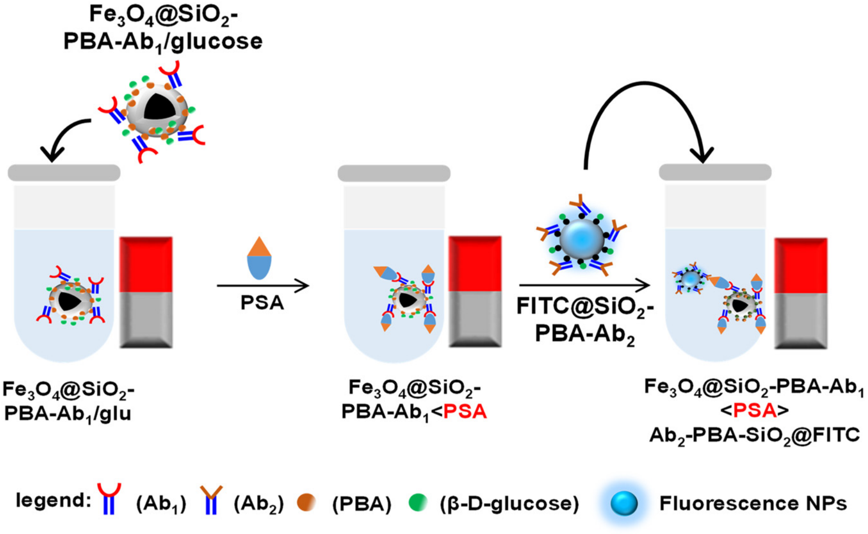

Scheme 2 Capture of PSA by Fe_3O_4@SiO_2-PBA-Ab_1/glucose and fluorescence detection using FITC@SiO_2-PBA-Ab_2/glucose.

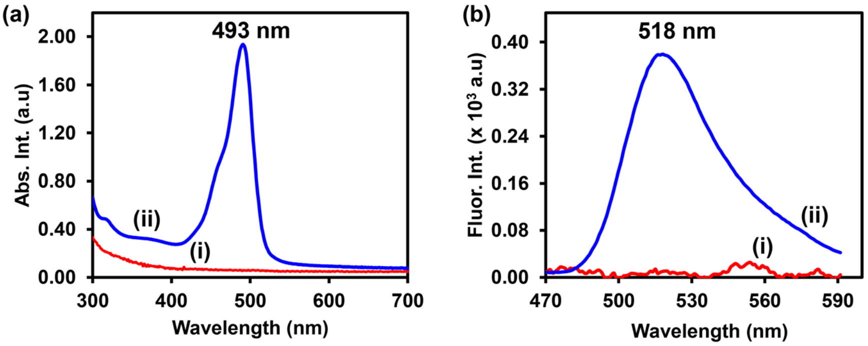

Fig. 6 (a) UV-vis absorption and (b) fluorescence emission spectra of (i) Fe_3O_4@SiO_2-PBA-Ab_1<PSA, and (ii) Fe_3O_4@SiO_2-PBA-Ab_1<PSA>Ab_2-PSA-PBA-SiO_2@FITC sandwich immunoassay.

shows the fluorescence intensity of the Fe_3O_4@SiO_2-PBA-Ab_1<PSA>Ab_2-PBA-SiO_2@FITC immunoassay at (a) different concentrations of Fe_3O_4@SiO_2-PBA-Ab_1/glucose and (b) the effects of the incubation time on the immunosensor response during the detection of PSA. The concentration of PSA was 50 ng mL^{-1} and FITC@SiO_2-PBA-Ab_1/glucose was 200 μg mL^{-1}. From Fig. S2(a),† the fluorescence emission intensity increased with increasing amounts of Fe_3O_4@SiO_2-PBA-Ab_1/glucose up to 100 μg mL^{-1}. Similarly, in Fig. S2(b)† the fluorescence emission intensity increased with increasing incubation time up to 50 minutes. The optimum incubation time after the immunoassay for the detection of FITC@SiO_2-PBA-Ab_1/glucose in 10 mM NaOH was 20 minutes at 37 °C. The high intensity was achieved after exposing the sandwich assay to 10 mM NaOH that hydrolyses the silica and releases the FITC molecules into the solution.

3.3 Detection of PSA

Using the proposed fluorescence immunosensor, PSA was detected using fluorescence measurements as shown in Scheme 2. The dissolution fluorescence-linked immunosorbent assay (dFLISA) method was employed for the detection of PSA. The sandwich immunoassay Fe_3O_4@SiO_2-PBA-Ab_1<PSA>Ab_2-PBA-SiO_2@FITC was exposed to a 10 mM NaOH (20 μL) solution for 20 minutes to hydrolyze the silica and release the FITC molecules. The solution was subjected to fluorescence measurements at an excitation of 480 nm. Fig. 7(a) shows the fluorescence emissions of varying PSA concentrations from 2.0 pg mL^{-1} – 100 ng mL^{-1}. The fluorescence emission intensity increased with increasing PSA concentrations. Fig. 7(b) shows the PSA dose–response curve for the correlation of the fluorescence intensity with an increase in the PSA concentrations. Fig. 7(c) shows the semi-log plot calibration curve of the proposed fluorescence immunosensor. The calibration curve of the change in fluorescence intensity Δ(Fluo. Int.)$_{max}$ = (Fluo. Int.$_i$ − Fluo. Int.$_o$) *vs.* the ln[PSA] was obtained over the linear concentration range from 2.0 pg mL^{-1} to 100 ng mL^{-1}. A linear regression equation with a regression coefficient (R^2) = 0.978 is shown in Fig. 7(c) and below eqn (2):

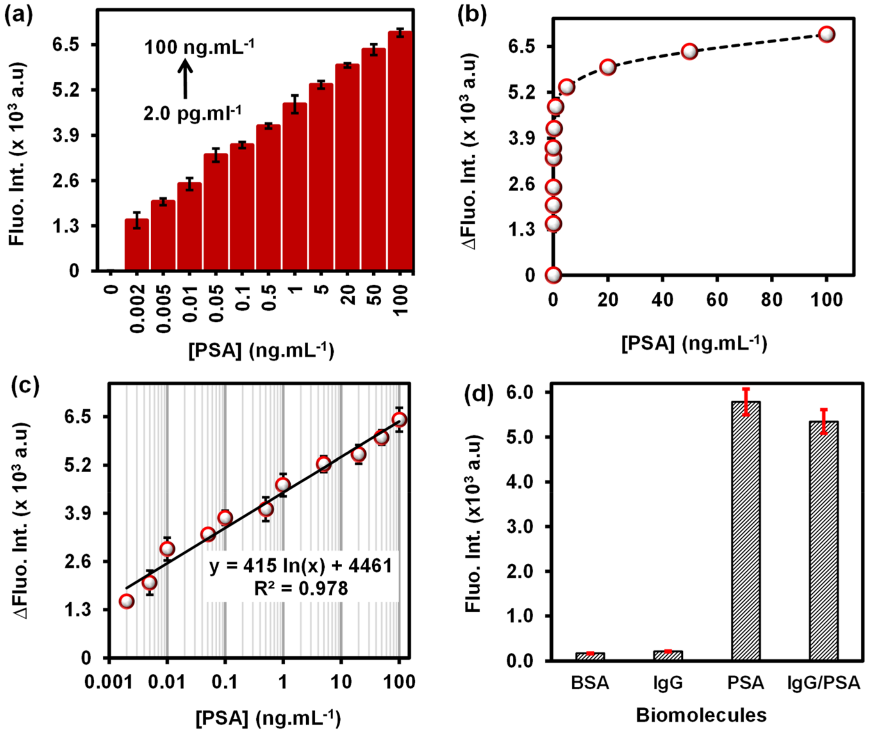

Fig. 7 (a) Bar graph of the fluorescence emission signal for different concentrations of PSA ranging from 2.0 pg mL^{-1} to 100 ng mL^{-1}. (b) Dose–response curve of relative fluorescence intensity ($\Delta FI_{max} = FI_i - FI_o$). (c) Linear relation of relative fluorescence intensity (ΔFI_{max}) against PSA concentrations, and (d) selectivity and specificity studies of the immunoassay sensor in the presence of PSA and other antibodies (n = 3).

$$\Delta(\text{Fluo. Int.})_{max} = 415\ln[\text{PSA}] + 4461 \quad (2)$$

A detection limit (LOD) of 0.81 pg mL^{-1} and a limit of quantification (LOQ) of 2.46 pg mL^{-1} were achieved and calculated using $3S/m$ and $10S/m$ (S = standard deviation of the blank and m = slope of the calibration curve). The results suggested that the fluorescence immunosensor can be used for sensitive detection of ultra-low concentrations of PSA. The applicability of the fluorescence immunosensor was studied in PSA spiked newborn calf serum (NCS) samples using the % recovery method. The average values of the % recovery and the coefficient of the variation (CV) results are summarized in Table S1.† A good recovery in the range of 98.0% to 102.7% was obtained, with a coefficient of variation (%CV) between 1.19% and 5.29%. These results show the reliability of the fluorescence immunosensor for PSA detection.

3.4 Specificity and selectivity of the immunosensor

The specificity and selectivity of the proposed immunosensor were investigated by determining the assay responses to PSA and other interfering analytes. Further, the real life application of the immunosensor was evaluated in newborn calf serum samples spiked with BSA, IgG antibody solutions and the mixture of IgG and PSA. Negative serum samples were used as blanks or negative samples with [PSA] = 0. The corresponding fluorescence response of the immunosensor, after removing the background interferences, are shown in Fig. 7(d). Fig. 7(d) shows the specificity and selectivity studies of the fluorescence immunosensor in the presence of PSA and other analytes like BSA and IgG, and a mixture of IgG and PSA. The IgG used is human IgG and not specific to PSA. From Fig. 7(d), the BSA and IgG antibody samples show very weak fluorescence response from trapped nanobioprobes during magnetic separation. The PSA and IgG + PSA spiked newborn calf serum samples gave high fluorescence intensity response. The immunosensor demonstrated excellent specificity and selectivity towards PSA detection. Furthermore, the comparison of the study was done with previously reported methods for detection for PSA as summarized in Table 1. The LOD of the study was found to be 0.81 pg mL^{-1} with an LOQ of 2.46 pg mL^{-1}. Compared to other previously reported methods for PSA detection, their LODs of 10 pg mL^{-1},[36] 3.0 pg mL^{-1},[8] 83 pg mL^{-1},[37] 27 pg mL^{-1},[38] and 30 pg mL^{-1}.[39] The previously reported methods employed the use of detection probes such as multi-CAT-AuNPs-Ab$_2$, HRP-Ab$_2$-SiO$_2$-NSs, CdTe@SiO$_2$-Ab$_2$, Ag/SiO$_2$@RuBpy@SiO$_2$-Ab$_2$, and rGO-Ca:CdSe-Ab$_2$, respectively. The proposed dFLISA immunosensor gave a lower LOD of 0.81 pg mL^{-1} for PSA detection. The proposed dFLISA in this study offered the advantage of using magnetic-silica capture nanobioconjugates for PSA concentration enrichment in the serum matrix and the highly fluorescent FITC-doped silica sensing nanobioprobes. The amplification of fluorescence signals was observed upon dissolution of the fluorescein–silica nanoparticles. The proposed method has many advantages especially considering very low concentrations of detected PSA by the proposed system and the

Table 1 A comparison of different analytical immunosensors' performance for the detection of PSA

Detection probe	Capture substrate	Signal monitored	Linear concentration range (LCR)	LOD
FITC@SiO_2-PBA-Ab_2/glucose[TW]	Fe_3O_4@SiO_2-PBA-Ab_1/glucose	Fluorescence	2.0 pg mL^{-1} – 100 ng mL^{-1}	0.81 pg mL^{-1}
CdTe@SiO_2-Ab_2 [8]	Fe_3O_4–Ab_1	Fluorescence	10 pg mL^{-1} – 5.0 ng mL^{-1}	3.0 pg mL^{-1}
HRP-Ab_2-SiO_2NSs[36]	Well/Ab_1/BSA	Fluorescence	30 pg mL^{-1} – 100 ng mL^{-1}	10 pg mL^{-1}
HRP-*anti*-PSA-IgG[37]	Well-anti-PSA-mIgY	Fluorescence	0.10–3.38 ng mL^{-1}	83 pg mL^{-1}
Ag/SiO_2@RuBpy@SiO_2-Ab_2 [38]	IMN-Ab_1	Photo-luminescence	0.10–100 ng mL^{-1}	27 pg mL^{-1}
Multi-CAT-AuNPs-Ab_2 [39]	MB-Ab_1	Colorimetric	50 pg mL^{-1} – 20 ng mL^{-1}	30 pg mL^{-1}

TW: this work; multi-CAT-AuNP-Ab_2: polyclonal goat anti-human PSA/catalase-labelled gold nanoparticles; HRP-Ab_2-SiO_2NSs: horseradish peroxidase-labelled anti-PSA antibody/silicon dioxide nanospheres; CdTe@SiO_2-Ab_2: PSA-labelled cadmium telluride@silica core–shell nanoparticles. HRP-anti-PSA-IgG: horseradish peroxidase-labelled anti-PSA antibody. Ag/SiO_2@RuBpy@SiO_2-Ab_2: a three layered silver core–shell, outer-layered RuBpy doped-silica fluorescent composite surface functionalized with the PSA antibody. IMN: immunomagnets.

scourge of prostate cancer worldwide. Future investigations will study the threshold and Gleason score of the modified system for early prostate cancer diagnosis. The only limitation of the system is the shelf life and long-term stability of the antibodies for selectivity and specificity of the immunosensor. These have limited shelf life (which is according to the supplier one year after the purchase). The storage and shelf life studies are part of our ongoing research activities.

4. Conclusions

In this work, we have developed a highly sensitive and selective fluorescence immunoassay for rapid detection of PSA using anti-PSA polyclonal antibody fluorescent-silica nanobioconjugates for fluorescence sensing and magnetic-silica antibody conjugates for PSA capture. The step-by-step preparation and characterization of the magnetic-silica antibody conjugates were successfully performed using microscopic and spectroscopic techniques. The preparation was successful as spherical magnetic-silica antibody capture nanobioconjugates were obtained. A sandwich immunocomplex of the fluorescein–silica sensing nanobioprobes and magnetic-silica capture nanobioconjugates formed through two immunoreactions used for the accurate detection of PSA. Compared with the ELISA method, the magnetic-silica capture nanobioconjugates assisted in PSA enrichment using a magnet to separate the captured PSA from the matrix. In addition, the fluorescent silica nanobioprobes enhanced the fluorescence intensity upon dissolution, using NaOH. This resulted in an amplified fluorescence signal due to the FITC molecules being released, enhancing the sensitivity of the immunoassay. The combined effects of the low background noise and increased fluorescence intensity resulted in a low limit of detection and limit of quantification in pg mL^{-1}. Moreover, the oriented bioconjugation of monoclonal and polyclonal PSA antibodies promoted specificity and selectivity to PSA. Potential interfering proteins could not be detected using this system confirming its specificity and selectivity even at higher concentrations. The presented immunoassay was simple, specific, and ultrasensitive for PSA detection in newborn calf serum samples (representing real samples). The specificity of the proposed method was due to the use of anti-PSA specific antibodies for PSA detection. Other immunosensors for specific biochemical targets or molecules can be adapted to this method.

Data availability

Data will be made available on request.

Author contributions

Tumelo Msutu: conceptualization, methodology, formal analysis, validation, data curation, investigation, writing – original draft, visualization. **Philani Mashazi**: conceptualization, methodology, validation, data curation, visualization, supervision, writing – review & editing, resources, project administration, funding acquisition.

Conflicts of interest

The authors declare no competing financial interest.

Acknowledgements

The authors would like to thank the National Research Foundation (NRF) for research funds through the NRF-STINT Bilateral (UID 118725) and NRF CPRR Grant supported this work. The authors also thank Rhodes University for research funding through Researcher Development Grant (RDG P5/17/2015), Rated Research Grant (RRG) and Sandisa Imbewu. TM thanks Gauteng City Regional Academy (GCRA) for an MSc Scholarship.

References

1 E. A. Stura, B. H. Muller, M. Bossus, S. Michel, C. Jolivet-Reynaud and F. Ducancel, *J. Mol. Biol.*, 2011, **414**, 530–544.
2 D. Damborska, T. Bertok, E. Dosekova, A. Holazova, L. Lorencova, P. Kasak and J. Tkac, *Microchim. Acta*, 2017, **184**, 3049–3067.
3 D. C. Pérez-Ibave, C. H. Burciaga-Flores and M.-Á. Elizondo-Riojas, *Cancer Epidemiol.*, 2018, **54**, 48–55.
4 H. Van Poppel, M. J. Roobol, C. R. Chapple, J. W. F. Catto, J. N'Dow, J. Sønksen, A. Stenzl and M. Wirth, *Eur. Urol.*, 2021, **80**, 703–711.

5 L. Yang, H. Zhao, G. Deng, X. Ran, Y. Li, X. Xie and C.-P. Li, *RSC Adv.*, 2015, **5**, 74046–74053.
6 P. Song, B. Yang, Z. Peng, J. Zhou, Z. Ren, K. Fang, L. Yang, L. Wang and Q. Dong, *Int. J. Surg.*, 2020, **76**, 64–68.
7 G. S. M. Kammeijer, J. Nouta, J. J. M. C. H. de la Rosette, T. M. de Reijke and M. Wuhrer, *Anal. Chem.*, 2018, **90**, 4414–4421.
8 Y. Zhao, W. Gao, X. Ge, S. Li, D. Du and H. Yang, *Anal. Chim. Acta*, 2019, **1057**, 44–50.
9 S. Veeranarayanan, A. Cheruvathoor Poulose, S. Mohamed, A. Aravind, Y. Nagaoka, Y. Yoshida, T. Maekawa and D. S. Kumar, *J. Fluoresc.*, 2012, **22**, 537–548.
10 M. D. Nguyen, H.-V. Tran, S. Xu and T. R. Lee, *Appl. Sci.*, 2021, **11**, 11301.
11 L. Zhang, H. Shao, H. Zheng, T. Lin and Z. Guo, *Int. J. Miner., Metall. Mater.*, 2016, **23**, 1112–1118.
12 R. C. Popescu, E. Andronescu and B. S. Vasile, *Nanomaterials*, 2019, **9**, 1791.
13 A. S. Teja and P.-Y. Koh, *Prog. Cryst. Growth Charact. Mater.*, 2009, **55**, 22–45.
14 L. Zhang, R. He and H.-C. Gu, *Appl. Surf. Sci.*, 2006, **253**, 2611–2617.
15 F. Ahangaran, A. Hassanzadeh and S. Nouri, *Int. Nano Lett.*, 2013, **3**, 23.
16 S. Mohapatra, N. Panda and P. Pramanik, *Mater. Sci. Eng., C*, 2009, **29**, 2254–2260.
17 C. Y. Wang, J. M. Hong, G. Chen, Y. Zhang and N. Gu, *Chin. Chem. Lett.*, 2010, **21**, 179–182.
18 N. V. Jadhav, A. I. Prasad, A. Kumar, R. Mishra, S. Dhara, K. R. Babu, C. L. Prajapat, N. L. Misra, R. S. Ningthoujam, B. N. Pandey and R. K. Vatsa, *Colloids Surf., B*, 2013, **108**, 158–168.
19 M. Bloemen, W. Brullot, T. T. Luong, N. Geukens, A. Gils and T. Verbiest, *J. Nanopart. Res.*, 2012, **14**, 1100.
20 Q. Fan, Y. Guan, Z. Zhang, G. Xu, Y. Yang and C. Guo, *Chem. Phys. Lett.*, 2019, **715**, 7–13.
21 S. Wang, J. Tang, H. Zhao, J. Wan and K. Chen, *J. Colloid Interface Sci.*, 2014, **432**, 43–46.
22 Z. Lu, J. Dai, X. Song, G. Wang and W. Yang, *Colloids Surf., A*, 2008, **317**, 450–456.
23 O. Adeniyi, S. Sicwetsha and P. Mashazi, *ACS Appl. Mater. Interfaces*, 2020, **12**, 1973–1987.
24 G. Asab, E. A. Zereffa and T. Abdo Seghne, *Int. J. Biomater.*, 2020, **2020**, 1–11.
25 A. Adesina, O. Adeniyi and P. Mashazi, *Electroanalysis*, 2023, **35**, 120–130.
26 S. Kralj, M. Drofenik and D. Makovec, *J. Nanopart. Res.*, 2011, **13**, 2829–2841.
27 P.-C. Lin, S.-H. Chen, K.-Y. Wang, M.-L. Chen, A. K. Adak, J.-R. R. Hwu, Y.-J. Chen and C.-C. Lin, *Anal. Chem.*, 2009, **81**, 8774–8782.
28 C. Bi, S. Zhang, Y. Li, X. He, L. Chen and Y. Zhang, *New J. Chem.*, 2018, **42**, 17331–17338.
29 T. Msutu, O. Adeniyi and P. Mashazi, *Sens. Diagn.*, 2024, **3**, 1167–1176.
30 R. Hufschmid, H. Arami, R. M. Ferguson, M. Gonzales, E. Teeman, L. N. Brush, N. D. Browning and K. M. Krishnan, *Nanoscale*, 2015, **7**, 11142–11154.
31 D. K. Kim and J. W. Lee, *J. Korean Ceram. Soc.*, 2018, **55**, 625–634.
32 J. M. Xu, Y. X. Zhang, G. H. Li, S. Wang, H. L. Ding and S. C. Xu, *Chem. Mater.*, 2012, **24**, 4572–4580.
33 R. M. Patil, P. B. Shete, N. D. Thorat, S. V. Otari, K. C. Barick, A. Prasad, R. S. Ningthoujam, B. M. Tiwale and S. H. Pawar, *RSC Adv.*, 2014, **4**, 4515–4522.
34 J. Nayeem, M. A. A. Al-Bari, M. Mahiuddin, M. A. Rahman, O. T. Mefford, H. Ahmad and M. M. Rahman, *Colloids Surf., A*, 2021, **611**, 125857.
35 C. Hui, C. Shen, J. Tian, L. Bao, H. Ding, C. Li, Y. Tian, X. Shi and H.-J. Gao, *Nanoscale*, 2011, **3**, 701–705.
36 L. Li, W. Zhang, Y. Wei, L. Yu and D. Feng, *J. Anal. Methods Chem.*, 2022, **2022**, 1–9.
37 A. Łupicka-Słowik, R. Grzywa, E. Leporowska, D. Procyk, J. Oleksyszyn and M. Sieńczyk, *Ann. Lab. Med.*, 2019, **39**, 373–380.
38 D.-D. Xu, Y.-L. Deng, C.-Y. Li, Y. Lin and H.-W. Tang, *Biosens. Bioelectron.*, 2017, **87**, 881–887.
39 Z. Gao, M. Xu, L. Hou, G. Chen and D. Tang, *Anal. Chem.*, 2013, **85**, 6945–6952.